Supplementary Material for Polarization-dependent single-pulse ultrafast optical switching of an elementary ferromagnet

Hanan Hamamera[1,2,*], Filipe Souza Mendes Guimarães[3], Manuel dos Santos Dias[1], and Samir Lounis[1,4,*]

[1]Peter Grünberg Institut and Institute for Advanced Simulation, Forschungszentrum Jülich & JARA, 52425 Jülich, Germany

[2]Department of Physics, RWTH Aachen University, 52056 Aachen, Germany

[3]Jülich Supercomputing Center, Forschungszentrum Jülich & JARA, 52425 Jülich, Germany

[4]Faculty of Physics, University of Duisburg-Essen & CENIDE, 47053 Duisburg, Germany

[*]h.hamamera@fz-juelich.de; s.lounis@fz-juelich.de

SUPPLEMENTARY FIGURES

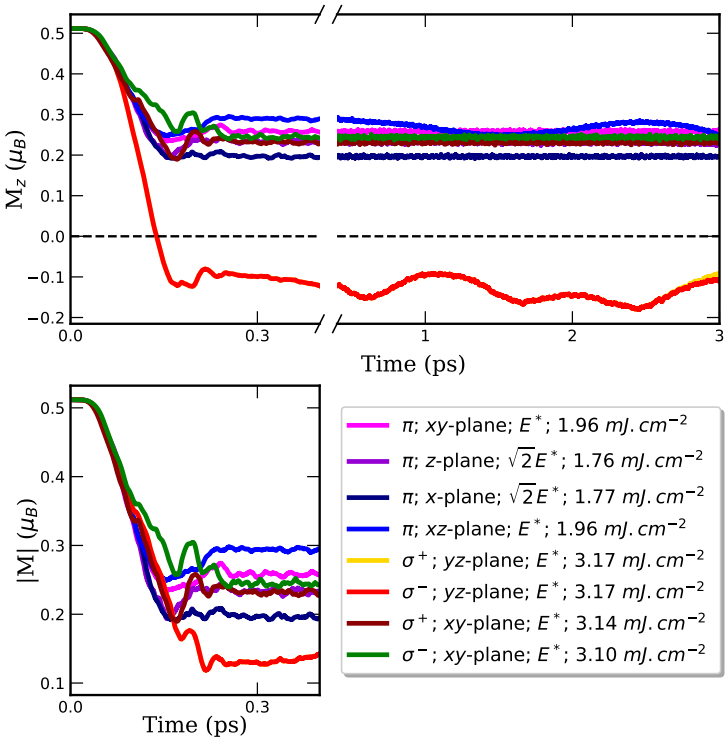

Supplementary Figure 1 | Diversity of laser-induced magnetisation dynamics for different polarisations. The responses of the Ni bulk magnetisation varies depending on the type polarizations, linear (π) or circular (σ), as well as in which direction or plane the electric field oscillates (indicated on the legend). The shapes of the pulse are given in Eqs. (4) and (5) of the main text. The reference value for the laser field intensity is $E^* = 9.7 \times 10^8\,\mathrm{V\,m^{-1}}$. The pulse has 300 fs width and the values of the electric-field intensity were chosen such that the maximum field is the same in all linear cases, which is $\sqrt{2}$ times larger than the circular ones. Even then, the response for a circular polarization in the plane that includes the initial polarization is the largest, as it also induces rotation of the magnetisation vector. The legend also indicates the corresponding absorbed laser fluence.

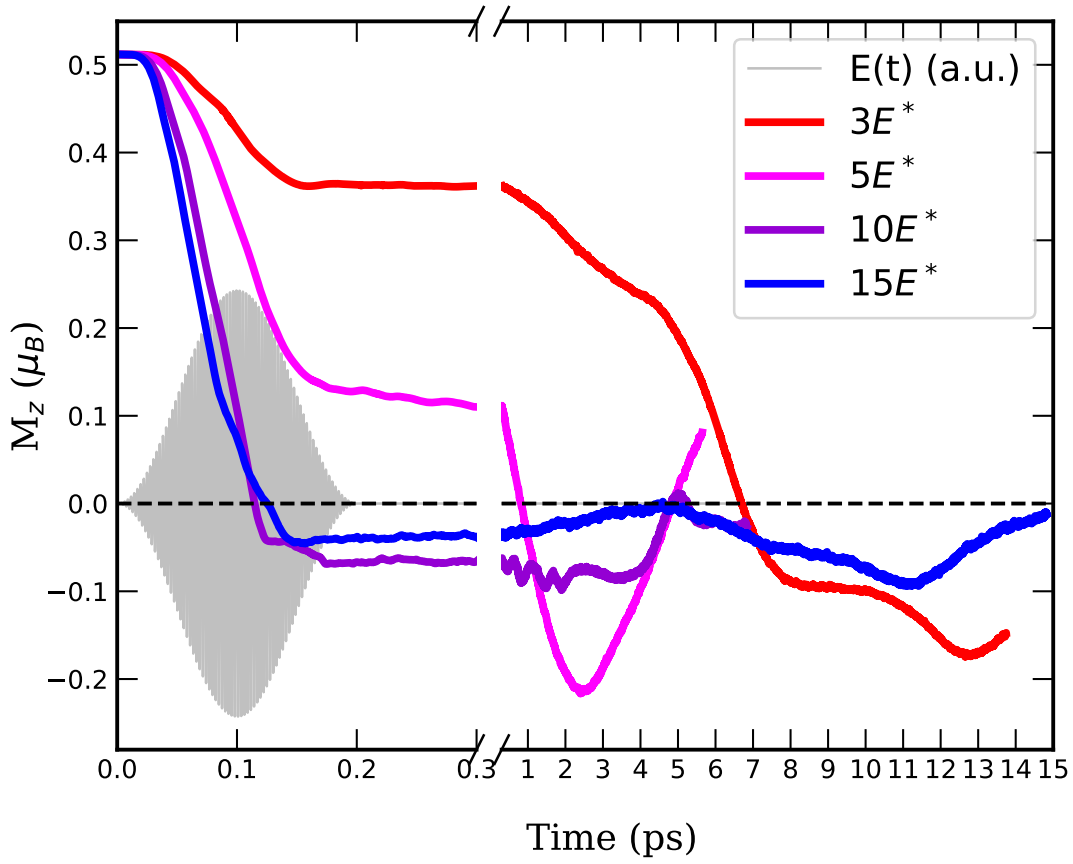

Supplementary Figure 2 | Magnetisation switching while the pulse still active. The $z-$component of the magnetization of Ni bulk present distinct behaviour when pumped with varied laser intensities $E^* = 9.7 \times 10^8\,\mathrm{V\,m^{-1}}$, and a fixed width of $200\,\mathrm{fs}$ (in grey). For higher field intensities (as the blue and violet curves), switching may occur while the pulse is still active.

SUPPLEMENTARY NOTES

Supplementary Note 1 | Theoretical approach

In this Note, we detail the methods used in our code—TITAN, developed to describe time-dependent transport and angular momentum properties in nanostructures [1–4]—, including how the ground state is obtained, as well as the propagation method we use to investigate the evolution of observables when a laser pulse is applied to the system. As Ni bulk has only one atom in the unit cell, the site indices are omitted.

Ground state The ground state of the system is described by the Hamiltonian

$$\mathcal{H} = \mathcal{H}_{\rm kin} + \mathcal{H}_{\rm xc} + \mathcal{H}_{\rm soc} \ , \tag{1}$$

where

$$\mathcal{H}_{\rm kin} = \frac{1}{N} \sum_{\mathbf{k}} \sum_{\mu\nu\sigma} t_{\mu\nu}(\mathbf{k}) \hat{c}^{\dagger}_{\mu\sigma}(\mathbf{k}) \hat{c}_{\nu\sigma}(\mathbf{k}) \quad , \tag{2}$$

is the tight-binding Hamiltonian describing the electronic hoppings, with $\hat{c}^{\dagger}_{\mu\sigma}(\mathbf{k})$ and $\hat{c}_{\nu\sigma}(\mathbf{k})$ being the creation and annihilation operators of electrons with spin σ and wave-vector $\mathbf{k}$ in the orbitals μ and ν, respectively. We employ an spd basis set. The tight-binding parameters $t_{\mu\nu}(\mathbf{k})$ were obtained by fitting paramagnetic band structures from first-principles calculations up to second nearest neighbors [5], within the two-center approximation [6]. N is the number of k-points in the full Brillouin Zone, which we use as an equally-spaced $22 \times 22 \times 22$ mesh.

The electron-electron interaction is characterized by a local Hubbard-like [7] interaction within

the Lowde-Windsor approximation [8], resulting in the mean-field exchange-correlation term

$$\mathcal{H}_{\rm xc} = -\frac{1}{N}\sum_{\mathbf{k}}\sum_{\substack{\mu\in d\\ \sigma\sigma'}}\frac{U}{2}\left\{m^{\alpha}\sigma^{\alpha}_{\sigma\sigma'} + \sum_{\nu\in d}\delta n_{\nu}\left(2\delta_{\sigma\sigma'}\delta_{\mu\nu} - \delta_{\sigma\sigma'}\right)\right\}c^{\dagger}_{\mu\sigma}(\mathbf{k})c_{\mu\sigma'}(\mathbf{k})\,. \tag{3}$$

Here, $U = 1.3\,\mathrm{eV}$ is the local effective Coulomb interaction [9], m^{α} and σ^{α} are the α-component of the magnetic moment vector (summed over the d orbitals) and of the Pauli matrix, respectively. δn_{ν} is the change in the occupation of orbital ν compared to the first principles calculations included in Eq. (2). m^{α} and δn_{μ} are determined self-consistently.

Finally, the coupling between the spin and orbital degrees of freedom are included in the d-electrons through an atomic spin-orbit interaction described by

$$\mathcal{H}_{\rm soc} = \frac{1}{N}\sum_{\substack{\mu\nu\\ \sigma\sigma'}}\sum_{\alpha}\lambda L^{\alpha}_{\mu\nu}S^{\alpha}_{\sigma\sigma'}\hat{c}^{\dagger}_{\mu\sigma}(\mathbf{k})\hat{c}_{\nu\sigma'}(\mathbf{k}) \quad , \tag{4}$$

where L^{α} and S^{α} are the α components of the orbital and spin angular momentum operators, respectively. The magnitude of the SOI λ is also obtained from first-principles calculations [10].

Real-time propagation The magnetic moments are excited by a laser pulse whose electric field is given by $\mathbf{E}(t) = -\mathrm{d}\mathbf{A}(t)/\mathrm{d}t$. The shapes of the vector potential for the different polarizations are given by Eqs. (4) and (5) of the main text. The Hamiltonian that describes the interaction with the laser can be written as

$$\begin{aligned}\mathcal{H}_{\rm laser}(t) &= -\int \mathrm{d}\mathbf{r}\ \hat{\mathbf{J}}^{\rm C}(\mathbf{r},t)\cdot\mathbf{A}(t)\\ &= -\frac{e}{\hbar N}\sum_{\mathbf{k},\sigma}\sum_{\mu\nu}\boldsymbol{\nabla}_{\mathbf{k}}t_{\mu\nu}(\mathbf{k})\cdot\mathbf{A}(t)c^{\dagger}_{\mu\sigma}(\mathbf{k},t)c_{\nu\sigma}(\mathbf{k},t) \quad .\end{aligned} \tag{5}$$

where $\hat{\mathbf{J}}^{\rm C}(\mathbf{r},t)$ is the current density operator, e is the electronic charge.

The evolution of the observables of the system are then obtained by first diagonalizing the ground state Hamiltonian $\mathcal{H}$ in Eq. (1), and then propagating the respective eigenvectors over time. The eigenvalues and eigenstates of the time-independent Schrödinger equation (at $t = 0$) are given by

$$\mathcal{H}|\psi^n(t=0)\rangle = E^n|\psi^n(t=0)\rangle \tag{6}$$

The pure states $|\psi^n\rangle$ can be written using a static basis set (in our case, the basis of local atomic orbitals used in the tight-binding model) $|\phi_i\rangle$ as

$$|\psi^n\rangle = \sum_i C_i^n|\phi_i\rangle \tag{7}$$

Inserting (7) into the time-dependent Schrödinger equation, one gets an equation for the time-dependent coefficients $C_i^n(t)$

$$-i\hbar\frac{\partial}{\partial t}\sum_i C_i^n(t)|\phi_i\rangle = \mathcal{H}(t)\sum_i C_i^n(t)|\phi_i\rangle \tag{8}$$

It is convenient to rewrite the coefficients $C^n(t)$ in terms of another set of $\tilde{C}_i^n$ given by $C_i^n = e^{\frac{-i}{\hbar}E^n t}\tilde{C}_i^n$ (which does not affect the probability density). With this modification, the time-dependent Schrödinger equation becomes

$$i\hbar\frac{\partial}{\partial t}\sum_i \tilde{C}_i^n(t)|\phi_i\rangle = (\mathcal{H}(t) - E^n)\sum_i \tilde{C}_i^n(t)|\phi_i\rangle \tag{9}$$

By making E^n as a reference, the evolution of the coefficients $\tilde{C}_i^n(t)$ becomes more stable, and also improves the variable step-size algorithm [11].

The time-dependent Schrodinger equation (9) is a first order differential equation of the form

$$\frac{\mathrm{d}y_\mu}{\mathrm{d}t} = f_\mu(t, y_1, ..., y_N) \tag{10}$$

with $\mathbf{y} = \psi$ and $\mathbf{f}(t, \mathbf{y}) = -\frac{i}{\hbar}\mathrm{i}[\mathcal{H}(t) + \mathcal{H}_{\text{laser}}(t)]\psi(t)$. Note that the application of the laser field causes changes to the magnetization and to the occupation, such that the exchange-correlation term in Eq. (3) becomes time-dependent, and $\mathcal{H}_{\text{xc}}(t)$ must be updated after every time step.

For a reliable prediction of the solution, the propagation method has to be symplectic, symmetric, and stable[12]. The symplecticity is associated with the notion of conservation of energy, while symmetry is related to time reversal. Stability refers to the dependence of the error on the integration step-size. If the method is insufficiently stable for a certain problem, the step size should be much smaller than the evolution of the solution for it to be accurate. This slows down the integrator and might reduce its efficiency when working with large systems [13]. Different methods can be used for step-size selection. One easy and flexible way is the use of two methods to estimate the local error. The method we have chosen uses an embedded pair of Runge-Kutta methods to save computational costs, namely the embedded-implicit Runge-Kutta method of fourth order (imRK4) [14].

In this method, the time interval $[t_0, t_1] = [t, t+h]$ is discretized into s steps (i.e., $t_i = t+c_i h$, $i = 1...s$). At the end of the interval, the method yields two solutions, y_1 and $\hat{y}_1$, that have the

following form:

$$y_1 = y_0 + h\sum_{j=1}^{s} b_j f\big(t_0 + c_j h, g_j\big) \tag{11}$$

$$\hat{y_1} = y_0 + h\sum_{j=1}^{s} \hat{b}_j f\big(t_0 + c_j h, g_j\big) \tag{12}$$

with the vector $g_i \in C^s$ satisfying

$$g_i = y_0 + h\sum_{j=1}^{s} a_{ij} f\big(t_0 + c_j h, g_j\big), \quad i = 1, \ldots, s \tag{13}$$

The coefficients c_i, b_i, $\hat{b}_i$ and a_i are given in the Butcher table (see Ref. 15).

The previous set of non-linear equations are then linearized using the Newton's iterative method [16]. The absolute difference between the two solutions is used in the calculation of errors and prediction of the new step size [17]. If the solutions are accepted (i.e., if they are inside the chosen margin of error), the obtained states representing one of the solutions $|\psi_{n,\mathbf{k}}(t)\rangle$ are used to calculate the expectation value of different observables as a function of time, as follows:

$$\langle \hat{O}(t) \rangle = \sum_{n,\mathbf{k}} f_{n,\mathbf{k}} \langle \psi_{n,\mathbf{k}}(t) | \hat{O}(t) | \psi_{n,\mathbf{k}}(t) \rangle. \tag{14}$$

Here $f_{n,\mathbf{k}}$ are the occupations of the eigenstates in the ground state according to the Fermi-Dirac distribution (which are kept constant), and the sub-notation (n,$\mathbf{k}$) runs over the number of electronic bands and the number of k-points, respectively, and indicates the original ground state wave function from which its time-evolved counterpart was obtained.

Supplementary References

1. Guimarães, F. S. M., Lounis, S., Costa, A. T. & Muniz, R. B. Dynamical current-induced ferromagnetic and antiferromagnetic resonances. *Phys. Rev. B* **92**, 220410 (2015). URL https://link.aps.org/doi/10.1103/PhysRevB.92.220410.

2. Guimarães, F. S. *et al.* Dynamical amplification of magnetoresistances and hall currents up to the thz regime. *Scientific reports* **7**, 1–9 (2017). URL https://www.nature.com/articles/s41598-017-03924-1.

3. Guimarães, F. S. *et al.* Comparative study of methodologies to compute the intrinsic gilbert damping: interrelations, validity and physical consequences. *Journal of Physics: Condensed Matter* **31**, 255802 (2019). URL https://iopscience.iop.org/article/10.1088/1361-648X/ab1239/meta.

4. Guimarães, F. S., Bouaziz, J., dos Santos Dias, M. & Lounis, S. Spin-orbit torques and their associated effective fields from gigahertz to terahertz. *Communications Physics* **3**, 1–7 (2020). URL https://www.nature.com/articles/s42005-020-0282-x.

5. Papaconstantopoulos, D. A. *Handbook of the Band Structure of Elemental Solids* (Springer US, Boston, MA, 2015). URL http://link.springer.com/10.1007/978-1-4419-8264-3.

6. Slater, J. C. & Koster, G. F. Simplified LCAO Method for the Periodic Potential Problem. *Phys. Rev.* **94**, 1498–1524 (1954). URL http://link.aps.org/doi/10.1103/PhysRev.94.1498.

7. Hubbard, J. Electron Correlations in Narrow Energy Bands. *Proceedings of the Royal Society A: Mathematical, Physical and Engineering Sciences* **276**, 238–257 (1963). URL https://royalsocietypublishing.org/doi/abs/10.1098/rspa.1965.0124.

8. Lowde, R. D. & Windsor, C. G. On the magnetic excitations in nickel. *Advances in Physics* **19**, 813–909 (2006). URL https://www.tandfonline.com/doi/abs/10.1080/00018737000101201.

9. Şaşıoğlu, E., Friedrich, C. & Blügel, S. Effective Coulomb interaction in transition metals from constrained random-phase approximation. *Phys. Rev. B* **83**, 121101 (2011). URL https://link.aps.org/doi/10.1103/PhysRevB.83.121101.

10. Thonig, D., Eriksson, O. & Pereiro, M. Magnetic moment of inertia within the torque-torque correlation model. *Sci. Rep.* **7**, 931 (2017). URL https://www.nature.com/articles/s41598-017-01081-z.

11. Völcker, C., Jørgensen, J. B., Thomsen, P. G. & Stenby, E. H. Adaptive stepsize control in implicit runge-kutta methods for reservoir simulation. *IFAC Proceedings Volumes* **43**, 523–528 (2010). URL https://www.sciencedirect.com/science/article/pii/S147466701630088X.

12. Gomez Pueyo, A., Marques, M. A., Rubio, A. & Castro, A. Propagators for the time-dependent kohn–sham equations: Multistep, runge–kutta, exponential runge–kutta, and commutator free magnus methods. *Journal of chemical theory and computation* **14**, 3040–3052 (2018). URL https://pubs.acs.org/doi/10.1021/acs.jctc.8b00197.

13. Jones, B. A. & Anderson, R. L. A survey of symplectic and collocation integration methods for orbit propagation (2012).

14. Butcher, J. C. *The numerical analysis of ordinary differential equations: Runge-Kutta and general linear methods* (Wiley-Interscience, 1987).

15. Rang, J. *Apdative Timestep Control for Fully Implicit Runge-Kutta Methods of Higher Order* (Univ.-Bibl., 2014). URL https://core.ac.uk/download/pdf/196658294.pdf.

16. Butcher, J. C. On the implementation of implicit runge-kutta methods. *BIT Numerical Mathematics* **16**, 237–240 (1976). URL https://link.springer.com/content/pdf/10.1007/BF01932265.pdf.

17. Hairer, E. & Wanner, G. *Solving Ordinary Differential Equations II: Stiff and Differential-Algebraic Problems (Springer Series in Computational Mathematics)* (Springer-Verlag Berlin Heidelberg, 2010). URL https://www.springer.com/de/book/9783540604525.